THE EFFECT OF FIN DESIGN ON THE INDUCED ROLLING MOMENT CHARACTERISTICS OF SOUNDING ROCKETS

W. Hatalsky, Manager, Aerodynamics
P. A. Sollow, Member Technical Staff
J. P. Taylor, Member Technical Staff
Space-General Corporation
9200 East Flair Drive
El Monte, California

Abstract

The importance of the effect of the induced rolling moments on roll pitch resonanceand roll lock-inphenomena has been long recognized. The intimate association of tail fin geometry withinduced rolling moments is established. In general, the experimental data presented indicate reduced rolling moments are minimized when the fin aspect ratio is increased. Adding an afterbody conical flare increases induced rolling moments. A nominal taper ratio near one-half has a beneficial effect in that experimental data indicates the induced rolling moment is minimized. Cruciform tail configurations are superior to triad tail assemblies because their induced rolling moments are smaller. These considerations are to be used in selecting tail fins which will contribute small induced rolling moments in the sounding rocket trajectory.

L Introduction

Perturbing a system at its natural frequency has the effect of introducing some extreme excursions in the system displacement. Roll-pitch coupling in sounding rockets is the precise same situation. When the natural frequency in pitch is the same as the roll rate, the angles of attack can attain large values. Associated with resonance phenomena is the roll lock-in which lunar-like motion occurs. A significant effect on the roll lock-in phenomena is exercised by the vehicle induced rolling moment characteristics.

Since a sounding rocket body is axisymmetric, the induced rolling moments are intimately related *to* the vehicle tail fins. By proper selection of tail fin proportions and cross-section, the magnitudes of the induced rolling moments can be reduced.

This paper will present the effect of some tail fin geometrical parameters on sounding rocket induced rolling moments. The data to be presented were determined from a series of wind tunnel tests performed at the Jet Propulsion Laboratory. Rolling moment data were gathered at supersonic and hypersonic speeds on a sensitive balance. The geometrical parameters covered are aspect ratio, taper ratio and sweep. Data are presented for both triad and cruciform tail arrangements.

The variations of the induced rolling moments are presented for angles of attack of a = 4°, 8°, and 12°, and at Mach numbers of M = 3, 5 and 8. The parametric variations of the data are not complete but are sufficient *to* establish significant trends in the data.

These rolling moment data have been used in performing six-degree-of-freedom trajectories for typical sounding rockets (Aerobee *350).* Typical six-degree-of-freedom digital computer trajectories are presented which illustrate the difficulties which can be encountered in the roll-pitch resonance region.

IL Symbols and Nomenclature

$AR = \frac{b^2}{2S_p}$ = aspect ratio (2 fins)

b = tail span (2 fins), inches (exposed)

$C_\ell = \frac{\mathcal{L}}{q\,Sd}$, general rolling moment coefficient

$C_{\ell_\delta} = \frac{\partial C_\ell}{\partial \delta}$ = partial derivative of rolling moment coefficient with respect *to* fin cant angle, 1/rad, 1/deg

$C_{\ell_i} = \frac{\mathcal{L}_i}{q\,S_p\,r}$ induced rolling moment coefficient

$P = \frac{\partial C_\ell}{\partial\left(\frac{pd}{2V}\right)}$ roll damping coefficient, 1/rad

Cm_a = pitching moment coefficient slope, 1/rad, 1/deg

c_R = tail fin root chord, in.

c_T = tail fin tip chord, in.

$c_4 = \frac{\partial C_\ell}{\partial \phi}$, 1/radian

d = body diameter, ft

$\eta = \sqrt{\alpha^2 + \beta^2}$ total angle of attack, deg.

I_x = roll moment of inertia, slug-ft^2

I_Y = pitch moment of inertia, slug-ft^2

$\mathcal{L}$ = rolling moment, in-lb, ft-lb

= induced rolling moment, in-lb, ft-lb

M = Mach number

$\mathcal{M}$ = pitching moment, ft-lb

$\mathcal{M}_\alpha$ = Cm_a q Sd = restoring moment, per unit. angle of attack, ft-lb/rad, ft-lb/deg

$\mathcal{N}$ = yawing moment, ft-lb

p = roll rate, rad/sec

$\dot{p}$ = roll acceleration, rad/sec^2

q = dynamic pressure, lbs/ft^2, lbs/in^2

r = body radius, in.

$\frac{r}{S_m}$ = body radius to body tail semispan ratio

S_p = fin planform area (one fin), in^2

S = body cross section area, ft^2

S_m = body tail semispan, in.

V = velocity, ft/sec

a = angle of attack, deg, rad.

ϕ = roll position angle, deg, rad.

$A = \frac{c_T}{c_R}$ = tail fin taper ratio

Ψ = tail fin leading edge sweep, degrees

$\omega = \sqrt{\frac{\mathcal{M}_\alpha}{I_y}}$, undamped natural freq., rad/sec

ϕ_{trim} = trimmed roll position angle, deg.

β = side slip angle, rad, deg.

III. Results and Discussion

For the present work, experimental data for 8 fin planforms were available. Seven of these planforms were used in triad tail configurations. The other one is for a cruciform tail configuration. A large part of the triad configuration data were gathered in a development contract for the Air Force Research Laboratory, Cambridge, Massachusetts. In this work, data were gathered from which a tail configuration was selected for the NLRO Sounding Rocket. The remaining data were gathered in the wind tunnel tests of the Aerobee 350, developed under the National Aeronautics and Space Administration sponsorship.

Figures 1 and 2 present the model scale dimensions of each of the tail panels and a pictorial representation of these tail panels. Table I presents the pertinent geometric parameters for each of the tail panels. In most instances these data were gathered for stability and performance data and the rolling moment data resulted as a by-product of this endeavor. As a result, the rolling moment data are not always of the accuracy which would be desired in the present application. In a small selection of tail fins, often more than one geometrical parameter is varied between two different tail panels. Under these circumstances, separating the effects of the different parameters is very difficult. The data which are presented are from References 1 through 7. The complete set of data available is not presented in Figures 1 and 2. Only the part of the available data to be used in this paper are presented.

The data in References 8 through 10 may be used to establish that a small induced rolling moment characteristic is in a direction to alleviate resonance problems. These references present both analytical and computational data to substantiate that reducing induced rolling moments is beneficial for sounding rocket trajectories.

Effect of Tail Panel Sweep

The effect of sweep on induced rolling moment is directly related to the generation of normal force on the tail panels. It is, in some instances, affected by the changes in interference between tail panels but this effect can occur only at relatively low Mach numbers and has been assumed to be a second order effect.

Figures 3 through 5 present induced rolling moment coefficient as a function of roll position angle at Mach numbers 3, 5, and 8. These data are for angles of attack at 4°, 8°, and 12°. The F_1 fin has a sweep angle of 48.7° and the F_2 fin a sweep angle of 38°.

Examining the data in Figures 3, 4, and 5, some unusual results are found. At a = 4°, M = 3, the fin with the larger sweep has a smaller average magnitude of induced rolling moment. For both sweep angles the only stable region for roll trim ($C_{\ell_\phi} < 0$) occurs between $\phi \approx 15°$ and 35°. There may be other regions at other angles of attack. At M = 5.04, a = 4°, a similar condition occurs except the differences between the average induced rolling moment coefficient values are small. At M = 8.03, a = 4°, the larger induced rolling moment average is for the fin which has the larger sweep. At the higher angles of attack for all three Mach numbers the induced rolling moments are much larger in magnitude. A typical crossplot of these data with angle of attack at small ϕ, i.e., 15°, would show small negative values at low angles of attack (a < 4°), a cross-over to positive values between a = 4° and a = 8° and an increasing positive value at a = 12°. At low angles of attack, the fin normal force and the resulting rolling moments are dominated by the fin lift characteristics and the body interference effects on the fin. At high angles of attack (a > 6°), the viscous cross-flow on the fins becomes dominant. The behavior of the data at a = 8° is not understood at this time.

The induced rolling moment coefficients in these graphs are based on the planform area of one fin and on the body radius.

From the examination of the effect of sweep on the induced rolling moments, it appears there is little difference due to sweep angles of 38° and 48.7°. If it were necessary to make a fin selection, it would be best to select the fin with the larger sweep for drag advantages.

Effect of Taper Ratio

One of the parameters available for varying the spanwise distribution of tail fin area is taper ratio. The effect of decreasing taper ratio is to redistribute the fin planform area inboard. The fins examined in this comparison are F_5, F_8, and F_9. In these comparisons the taper ratio varies from

$\lambda = .219$ to $\lambda = .646$. The comparisons must be made in two steps. The first is a comparison of fins F and F_9. In this case, the span and sweep is held constant and the fin area therefore varies with λ. Since the rolling moment coefficient is based on fin planform area this effect has been normalized. As a result the comparison is a valid one. The second comparison is of fins F_5 and F_8. In this instance, the span and area are held constant and a change in sweep accompanies the change in taper ratio. Here the change in sweep is from $\Psi = 48.7^{\circ}$ to $\Psi = 59.4^{\circ}$. Since this sweep effect was shown to be a small one in a previous section, the variation is primarily one of taper ratio. As a result, a comparison of all three sets of data is legitimate and the only significant parameter may be interpreted to be the taper ratio.

Figures 6 through 9 present induced rolling moment coefficient as a function of roll position angle for taper ratios of $\lambda = .219$, .46, and, 646. These data are for Mach numbers M = 3.01 and 5.06 and angles of attack of $a = 4^{\circ}$, 8°, and 12°. At $a = 4^{\circ}$, M = 3.01, the taper ratio of $\lambda = .46$ has the lowest induced rolling moment. At M = 5.06, $a = 4^{\circ}$, all three taper ratios have very small induced rolling moments with $\lambda = .646$ having the smallest. At $a = 8^{\circ}$, M = 3.01, $\lambda = .646$ is low, at M = 5.06, $\lambda = .46$ is the lower. At $a = 12^{\circ}$, M = 3.01, $\lambda = .219$ is low, at M = 5.06, $\lambda = .46$ is the lowest. The variation in taper ratio for the lowest induced rolling moment indicates that the factors are changing in a complex manner. In eight of the nine cases presented the lower taper ratio near $\lambda = .500$ had the lower induced rolling moment. As a result, it may be concluded that reducing taper ratio will likewise reduce induced rolling moment.

Effect of Aspect Ratio

From Figure 1, the three fins selected to illustrate the effect of aspect ratio are F_1, F_4, and F_5. Although aspect ratio is shown as the important variable, these fins are demonstrating the effect of a change in span. This is because a change in area and moment arm accompanies the change in aspect ratio. The experimental induced rolling moment data for fins F_1, F_4, and F_5 are presented in Figures 10 through 15. Presented is rolling moment coefficient as a function of roll position angle, ϕ, for Mach numbers M = 301, 5.04, and 8.03. These data are presented at angles of attack of $a = 4^{\circ}$, 8°, and 12°.

Examining the data in the low angle of attack range indicates that at the low Mach numbers (M = 3.01) the tail configuration with the large span or high aspect ratio has the lowest induced rolling moments. At the high Mach numbers (M = 8.03), the short span or low aspect ratio fins has the lower induced rolling moment. At the intermediate Mach number ($M \approx 5$), the span or aspect ratio doesn't seem to make any difference. This change is attributed to the tail fins intersecting the bow shock wave. As a rule of thumb, it appears that increasing the aspect ratio or fin span as much as possible without intersecting the bow shock results in the lowest induced rolling moments. As a result, it is concluded that increasing span or aspect ratio is in the direction to reduce rolling moments as long as the bow shock limitation is observed.

Effect of Afterbody Flare on Induced Rolling Moment

One of the items not immediately amenable to analysis but for which experimental data are available in References 1 through 7 is afterbody flare. Tail assemblies F_6 and F_7 have a 3 degree conical flare over the aft 74% of the root chord. By comparing the rolling moment coefficient data for configuration B_1 F_1 and B_1 F_6, the effect of the flare on the induced rolling moment can be determined. These data are presented in Figures 16 to 19 for Mach numbers 5.04 and 8.03 and for angles of attack of 4, 8, and 12 degrees. Examination of these data indicates that in the majority of the six plots the configuration with the flare had the highest induced rolling moment. The magnitude of the increase appears to be approximately 5 to 15% at the peak values.

Comparison of Induced Rolling Moments of Triad and Cruciform Tail Vehicles

A significant preliminary variable has been neglected in the foregoing discussion. This is the triad versus the cruciform tail configuration. An early selection of a three finned or four finned tail configuration can make a definite contribution to reducing induced rolling moment coefficients. In the tail configurations presented in Figures 1 and 2, Fin F_5 and Fin F_{11} are most easily compared. These fins have geometrical characteristics which are very similar except one is for a three finned assembly (F_5), the other is for a four finned tail assembly. The geometric parameters for both are presented below.

Fin	Ψ	S_p	AR	r/S_m	λ	t/c	$(\frac{\ell}{d})$ body
F 5	48.7	5.9	2.099	.208	.46	.0932	22.6
F 11 (A/B 350)	45	4.5	1.81	.244	.50	.1048	21.2

As can be seen, these fin panels are very similar. In no case is any one parameter different by more than 10% between the two fins. On this basis, the data are considered comparable enough to indicate the relative magnitudes of the induced rolling moments.

The data are presented in Figures 20 through 23. These figures present rolling moment coefficient as a function of roll position angle. As can be seen there are two sets of values on the abscissa. This is because the triad tails have a period of 120 degrees, while the cruciform have a period of 90°. The data presented are for the first half period for both configurations. The triad tail configuration has the lower induced rolling moment in the majority of the data presented. This is an expected for the boundary conditions imposed on this comparison. At $\phi = 0^{\circ}$, the triad tail configuration has two fins on the windward side of the body, but both are at a 30" angle relative to a horizontal plane. As a result of their lifting capacity is reduced to $(\cos^2 30^{\circ})$ or three quarters of two similar tail fins inahorizontal plane. By this reasoning the induced rolling moments of the triad tails in Figures 20 through 23 should be increased by 33%. Using this approximatevalue, the triad tails will stili have the lower induced rolling moments by approximately 20% at M = 3 for $a = 4^{\circ}$ and 8°. At M = 5, the cruciform tail will have a lower induced rolling moment by approximately 10% (M = 5, $a = 8^{\circ}$). On this basis, it appears the triad tail fin has the lower induced rolling moment when considering the same panel lift. When the panel lift is increased on the triad fins to obtain the same lift in the vertical plane as the cruciform fins produce,

the triad tails have a lower induced rolling moment at M = 3, but at M = 5, the cruciform fins seem to have a slightly lower induced rolling moment.

Six-Degree-of-Freedom Trajectories

In order to illustrate the manner in which a variation of the induced rolling moment affects the flight dynamics of a vehicle, two cases have been selected from a study performed previously by Space-General Corporation. Two of these studies (References 10 and 11) were performed to computerized simulations of trajectories flown with various space and body-fixed perturbations and varied aerodynamic coefficients. A six-degree-of-freedom program with quasi-steady aeroelastic representation was employed for all of the trajectories. The vehicles which were studied were the Aerobee 150 (three-finned), and the newer and larger four-finned Aerobee 350. Two cases from the Aerobee 350 study are presented here. The Aerobee 350 study served to show not only that realizable wind profiles could not, by themselves, introduce lock-in, but could moreover be expected to reduce the likelihood of a sustained lock-in. This is due to the fact that the lock-in condition requires a rather delicately balanced moment equilibrium, which would be upset if some variation in the wind vector caused an angle of attack perturbation. It was also shown that fin and thrust misalignments would cause roughly equivalent lock-ins if they produced equal disturbing moments just prior to the nominal resonance. On the basis of these findings, it was concluded that thrust misalignment could be properly and expeditiously selected as the sole perturbation when investigating the susceptibility of a particular configuration to roll lock-in. It must be emphasized that this is not to say that only thrust misalignments will cause roll lock-in, but only that body-fixed perturbation of the same magnitude (moment) would be necessary to cause lock-in.

The Aerobee 350 study showed that thrust misalignments on the order of 1.7 degrees would be required to produce lock-in with the nominal aerodynamic configuration. Since this is an extremely large misalignment, and equivalent to a very large disturbing moment from whatever source, it is apparent that the lock-in susceptibility of this configuration is quite low.

The sample between Aerobee 350 cases, taken from Reference 10, included a 1.6 degree thrust misalignment at an orientation relative to the body axes such that the misalignment moment vector was rotated 20 degrees counterclockwise, looking forward, from the body y-axis.

The two cases differ only in the magnitude of the induced rolling moment coefficient. Case 13 included the values of this coefficient which were derived from wind tunnel data while Case 45 included twice the nominal values. It may be seen from the histories of the relative roll orientations in the neighborhood of resonance (Figure 24), that roll lock-in occurred in Case 45, but not in Case 13. The roll rate histories (Figure 25) show perturbations in the roll rate for both cases, with the much more pronounced departure from the nominal history occurring in Case 45. It is interesting to note that the spin rate during lock-in does not follow the linear aerodynamic natural frequency (ω_o). It was determined, from this and the subsequent study of the Aerobee 150 that the spin rate locked to a frequency $\omega_i \cos \eta$ where ω_i, the instantaneous natural frequency, is given by $\sqrt{-M/T_y}\,\eta$ (radians/second). This differs from the linear natural frequency $\sqrt{-(dM/d\eta)/I_y}$, with the difference increasing with increasing angle of attack. At resonance (near t = 30 seconds), the angle of attack is still small (Figure 26), so that lock-in appears to occur at p = ω. It may be seen from Figure 26 that the angle of attack histories are quite similar until 32 seconds, by which time Case 45 has been locked-in for two seconds. After this time, the angle of attack of Case 45 increases somewhat while that of Case 13 decays rapidly. It is interesting to note that the maximum angle of attack experienced in Case 45 occurs after the termination of lock-in (after 34 seconds). This contrasts with the catastrophic yaw described in Reference 8. The expression for amplification factor (η/η_{trim}) from Reference 10, shows that depending on the sign of the induced yawing moment, $\eta(\alpha, \phi')$, this moment may either reinforce or negate the damping. It has been found that for the slender finned sounding rocket configurations investigated, this moment always decreases the amplification factor when the vehicle is in a roll orientation where stable lock-in is possible and increases it at other roll orientations. Thus, immediately after breakout, the amplification factor of Case 45 increases markedly.

These two sample cases graphically illustrate the effect which variations of the magnitude of the induced rolling moment, independent of any other configurational changes, have on the susceptibility of a vehicle to roll lock-in.

IV. Recommendations and Conclusions

From the analysis of experimental test data, the following trends have been established in relation to induced rolling moments.

1. Tail assemblies with lower induced rolling moments are less susceptible to roll lock-in.
2. Reducing fin taper ratio is in a direction to reduce induced rolling moment.
3. Increasing fin aspect ratio will tend to reduce induced rolling moment (as long as the fins remain within the bow shock).
4. Placing a conical flare under triad tail fins tends to increase the induced rolling moments in the magnitude of 10%.
5. Triad tail assemblies ,have lower induced rolling moments at M ≈ 3 for both the same panel lift and the same normal force. At Mach numbers near M = 5, the cruciform has a slight advantage.
6. Over the range of sweep angles from $\Upsilon = 38^\circ$ to $\Upsilon = 48.7^\circ$, there are small differences in rolling moments.
7. The area of induced rolling moments on sounding rockets is a fertile area for additional research.

V. References

1. JPL WT 21-181, "Test of the Space-General Aerobee 150 Model in the JPL 20-Inch Supersonic and 21-Inch Hypersonic Wind Tunnels': by W. J. Marko, May 1965.
2. JPL WT 20-593, "Test of the Space-General Nike Iroquois Model in the JPL 20-Inch Supersonic Wind Tunnel", by W. J. Marko, May 1965.
3. JPL WT 20-576, "Test of the Space-Genera? Nike Iroquois Model in the JPL 20-Inch Supersonic. Wind Tunnel", by M. J. Argoud, Mag 1964.

4. JPL 21-145, "Testpf the Space-General Nike-Iroquois in the JPL 21-Inch Hypersonic Tunnel", by M. J. Argoud, March 1964.
5. JPL 21-168, "Test of the Space-General Nike Iroquois in the JPL 21-Inch Hypersonic Wind Tunnel", by M. J. Argoud, July 1964.
6. Report No. 1784, "Wind Tunnel Tests of the Aerobee 150A (Model AJ60-13)" by E. S. Thomas, May 1960.
7. JPL WT 20-587, "Test of the Space-General Aerobee 350 Model in the JPL 20-Inch Supersonic Wind Tunnel", by M. J. Argood, July 1964.
8. IAS Report No. 59-17, "Two Non-Linear Problems in the Flight Dynamics of Modern Ballistic Missiles", by J. D. Nicolaides, January 1959.
9. AIAA Paper No. 66-463, "An Approximate Solution for the Near-Resonant Motion of a Canted-Fin Sounding Rocket Vehicle", by James E. Brunk, June 1966.
10. SGG Report 379RC-2 (Volumes I, II, III), "Aerobee 350 Roll-Yaw Coupling Study", by P. A. Sollow. December 1964,
11. SGC Report 785FR-2, "Aerobee 150 Roll Lock-in Susceptibility Study Using the SGC six-Degree-of-Freedom Trajectory Simulation Computer Program", P.A. Sollow, July 1965.

Fin	Tail	Fins in Assy	Sweep (°)	Original Data $S_{Ref}(in^2)$	Original Data ℓ_{Ref} (in)	S_p (in^2)	AR	$\frac{r}{S_m}$	λ	b (in)
1	F_1	3	48.7	7.42	.65	7.42	2.644	.1712	.46	3.136
2	F_2	3	38.0	7.42	.65	7.42	2.644	.1712	.46	3.136
3	F_4	3	48.7	9.oil	.65	9.0	3.192	.147	.46	3.786
4	F_5	3	48.7	5.90	.65	5.90	2.099	.208	.46	2.486
5	F_6*	3	48.7	7.42	.65	7.42	2.644	.1712	.46	3.136
6	F_8	3	j9.4	5.898	.65	5.898	2.099	.208	.219	2.486
7	F_9	3	48.7	6.648	.65	6.648	1.865	.208	.646	2.486
8	A/B 350	4	45	1.328	1.30	4.50	1.81	.244	.500	2.021

*Tail Panel F6 has a 3° Conical Flare over 74% of the Root Chord

Table 1. Tail Fin Geometric Characteristics

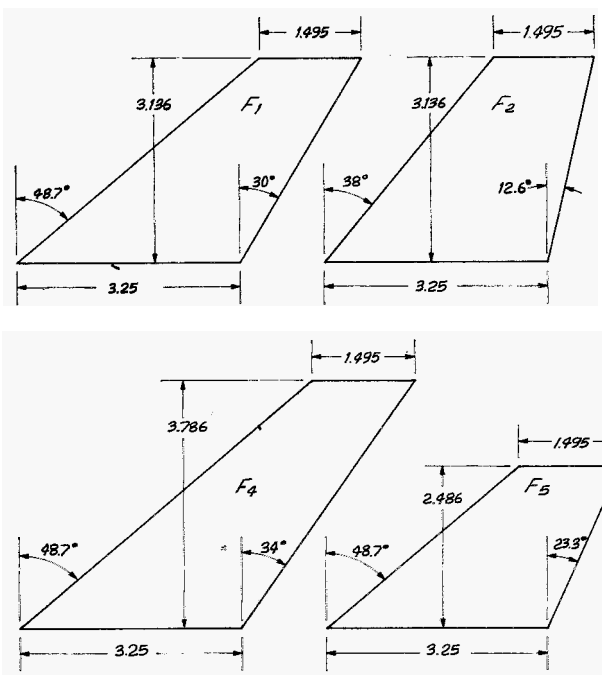

Figure 1. Tail Fins Used in Rolling Moment Analysis - Three Fins in Assembly

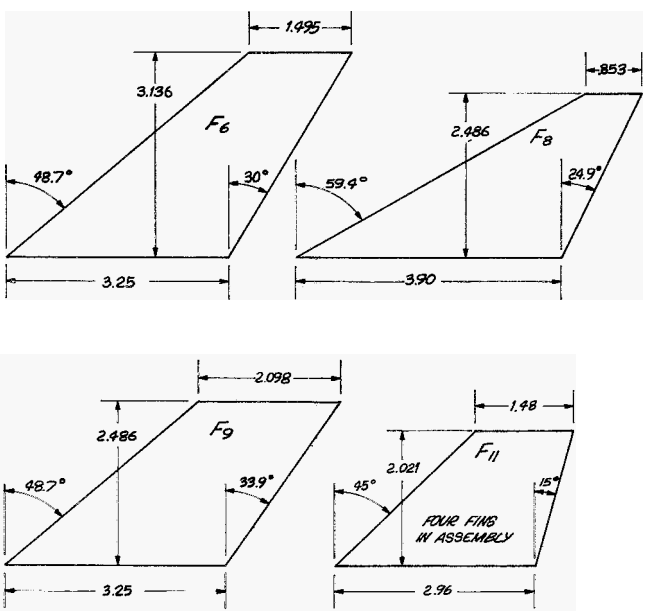

Figure 2. Tail Fins Used in Rolling Moment Analysis - Three Fins in Assembly

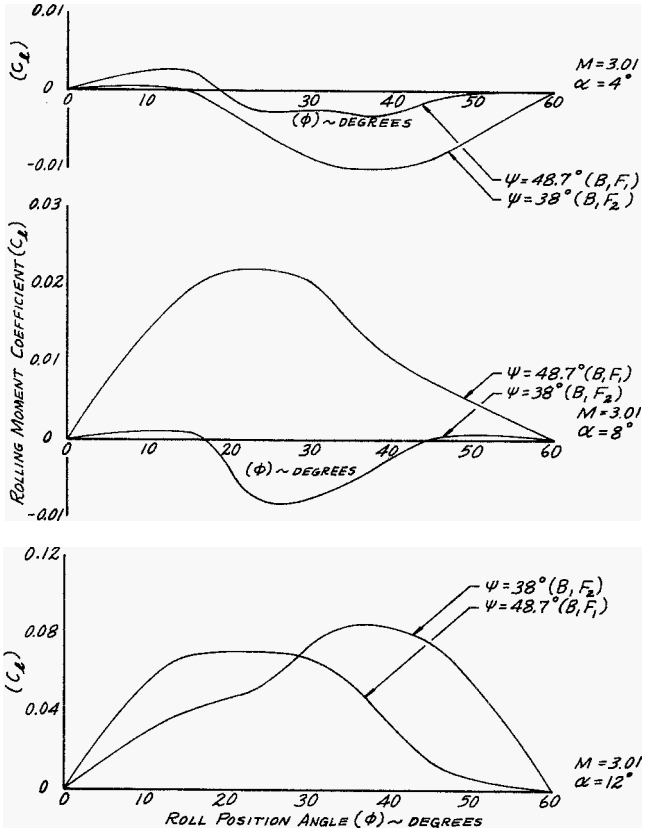

Figure 3. Effect of Leading Edge Sweep on Induced Rolling Moment
S_{REF} = Planform Area of One Fin
ℓ_{REF} = Body Radius

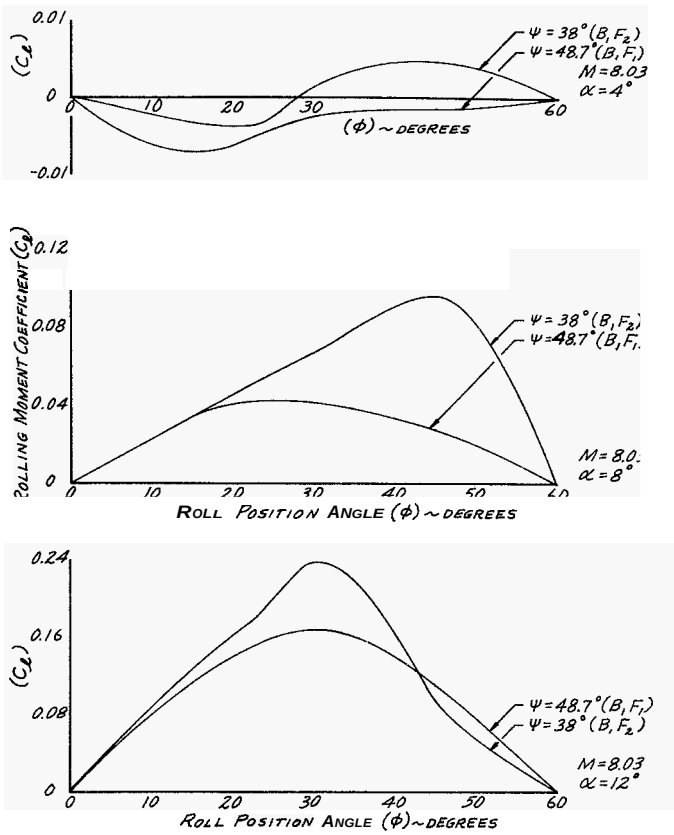

Figure 4. Effect of Leading Edge Sweep on Induced Rolling Moment
S_{REF} = Planform Area of One Fin
ℓ_{REF} = Body Radius

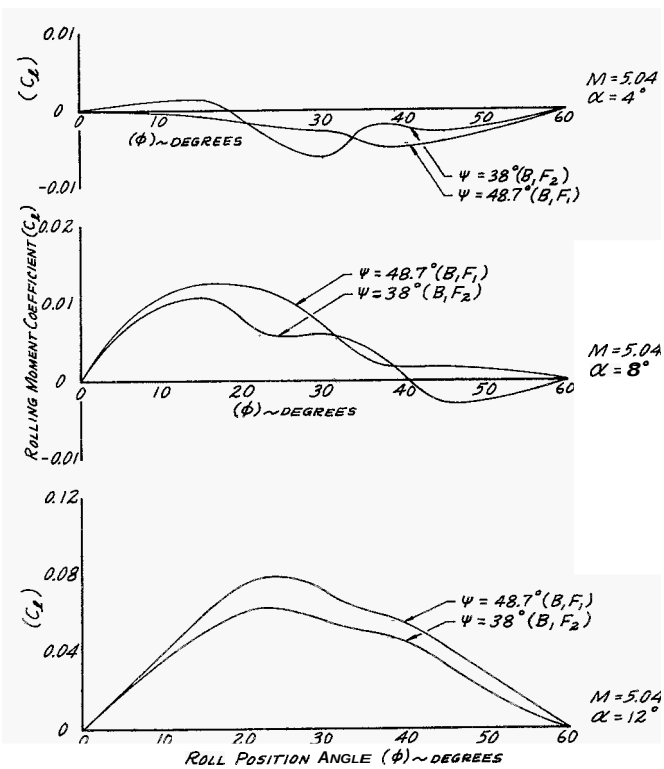

Figure 5. Effect of Leading Edge Sweep on Induced Rolling Moment
S_{REF} = Planform Area of One Fin
ℓ_{REF} = Body Radius

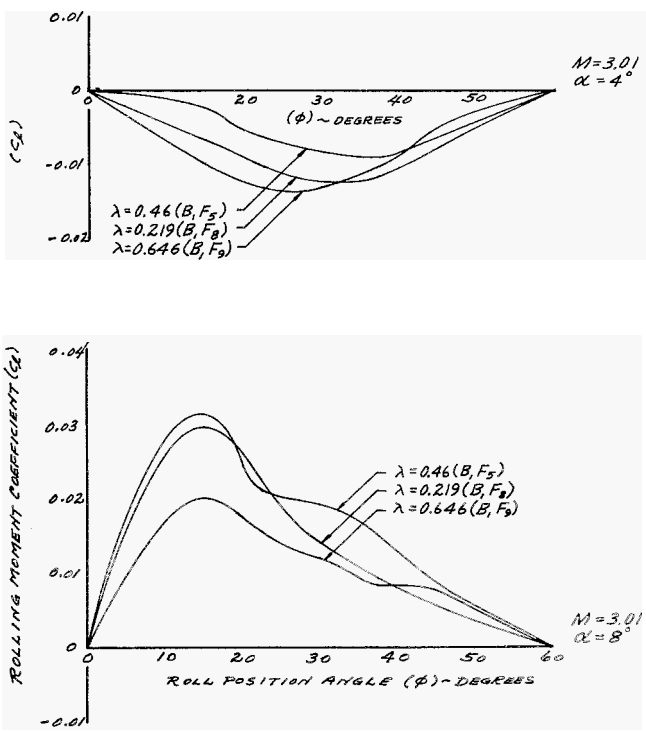

Figure 6. Effect of Taper Ratio on Induced Rolling Moment
S_{REF} = Planform Area of One Fin
ℓ_{REF} = Body Radius

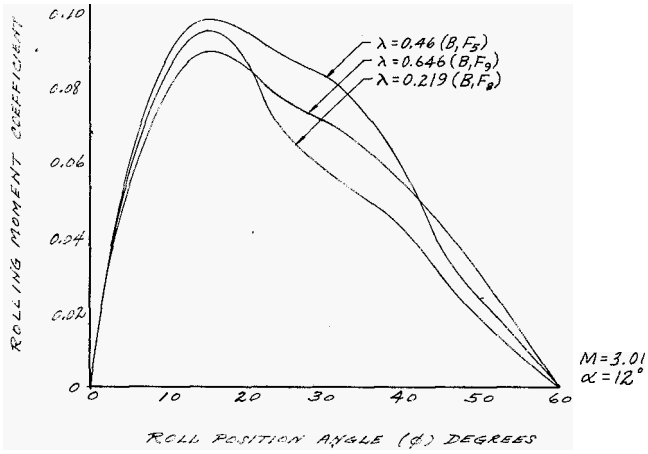

Figure 7. Effect of Taper Ratio on Induced Rolling Moment
S_{REF} = Planform Area of One Fin
ℓ_{REF} = Body Radius

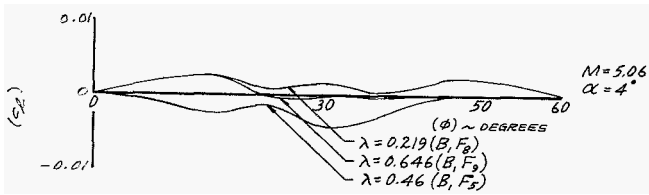

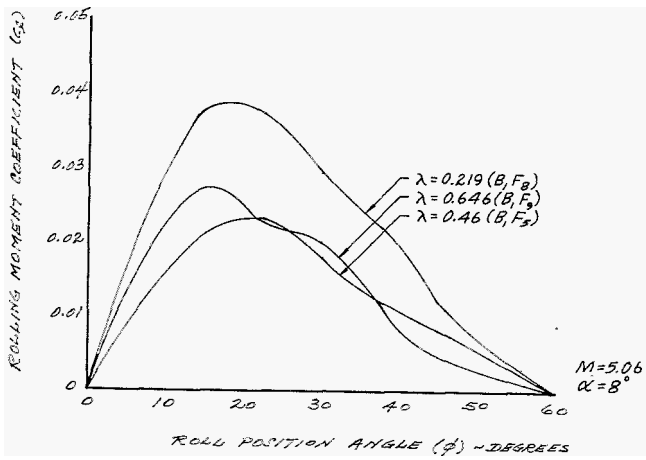

Figure 8. Effect of Taper Ratio on Induced Rolling Moment
S_{REF} = Planform Area of One Fin
ℓ_{REF} = Body Radius

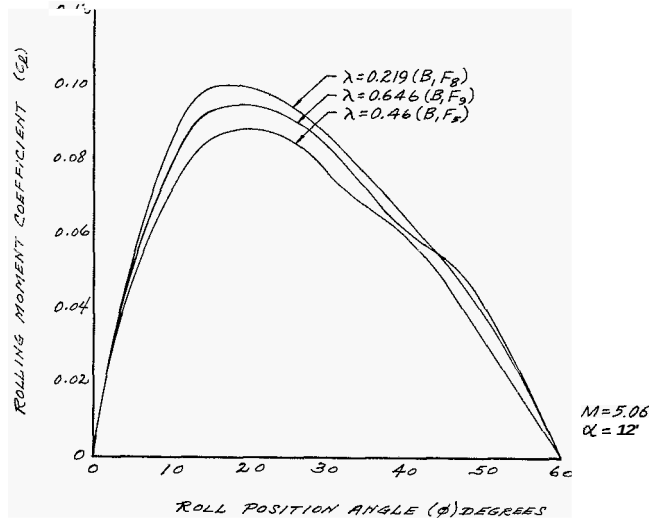

Figure 9. Effect of Taper Ratio on Induced Rolling Moment
S_{REF} = Planform Area of One Fin
ℓ_{REF} = Body Radius

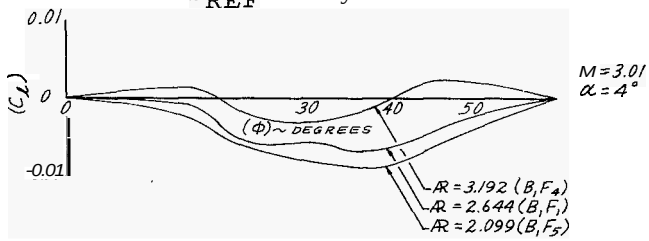

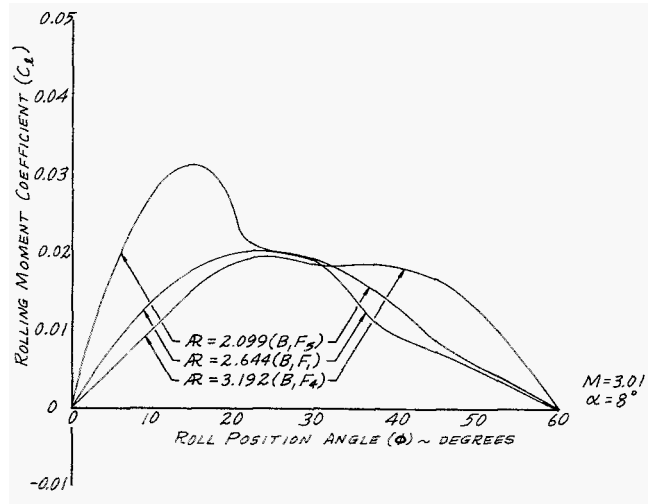

Figure 10. Effect of Aspect Ratio on Induced Rolling Moment
S_{REF} = Planform Area for One Fin
ℓ_{REF} = Body Radius

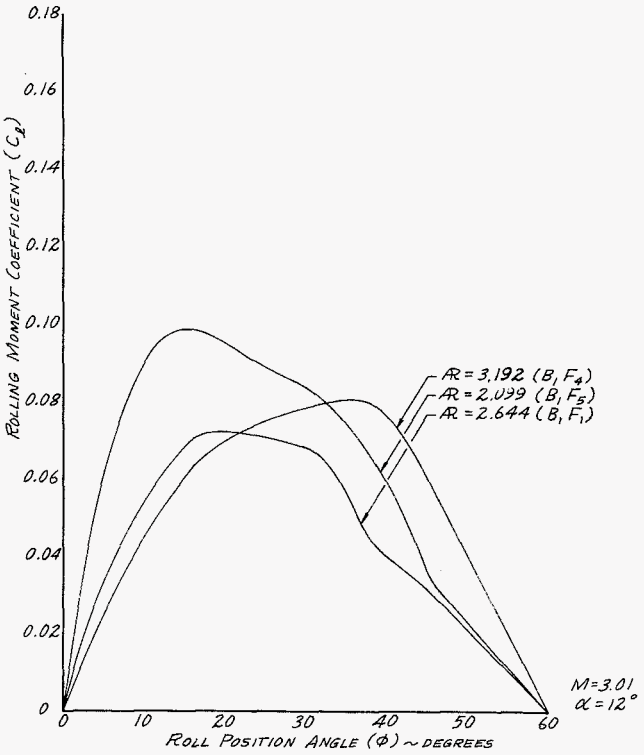

Figure 11. Effect of Aspect Ratio on Induced Rolling Moment
S_{REF} = Planform Area for One Fin
ℓ_{REF} = Body Radius

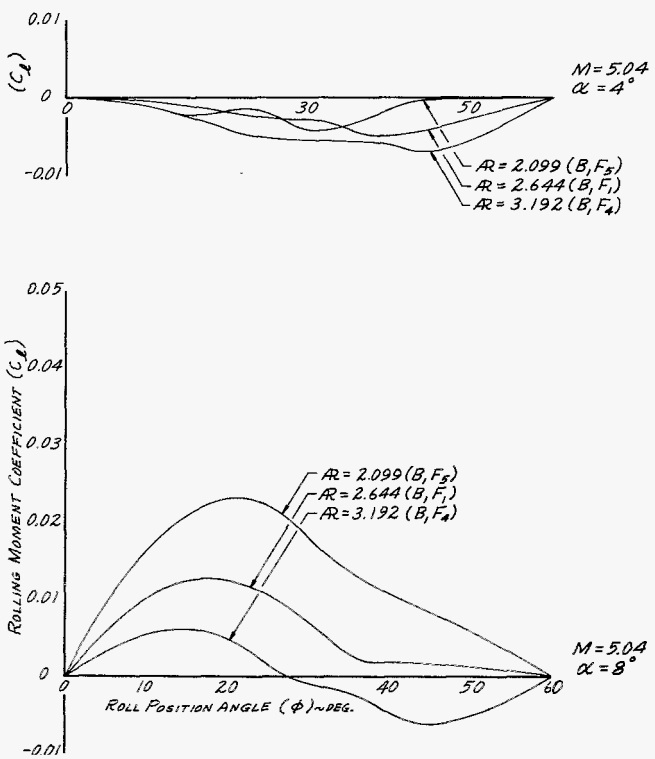

Figure 12. Effect of Aspect Ratio on Induced Rolling Moment
S_{REF} = Planform Area for One Fin
ℓ_{REF} = Body Radius

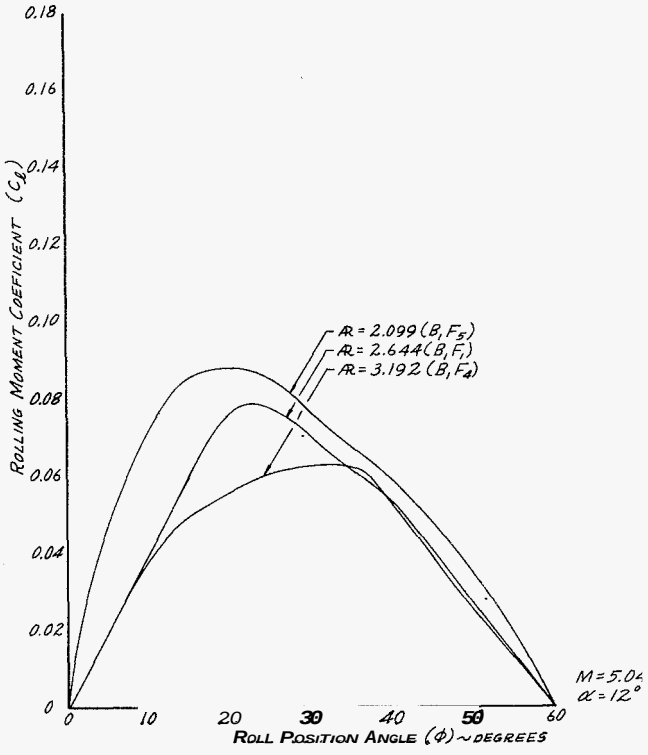

Figure 13. Effect of Aspect Ratio on Induced Rolling Moment
S_{REF} = Planform Area for One Fin
ℓ_{REF} = Body Radius

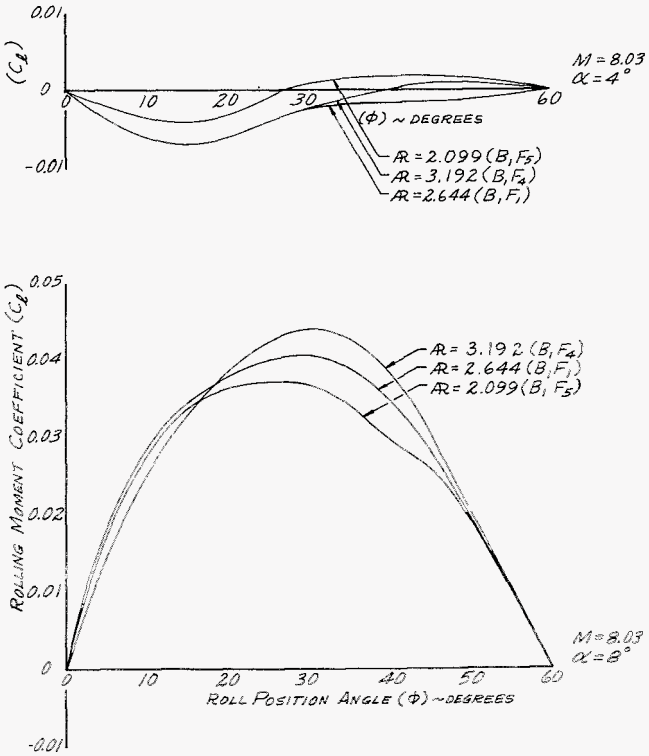

Figure 14. Effect of Aspect Ratio on Induced Rolling Moment
S_{REF} = Planform Area for One Fin
ℓ_{REF} = Body Radius

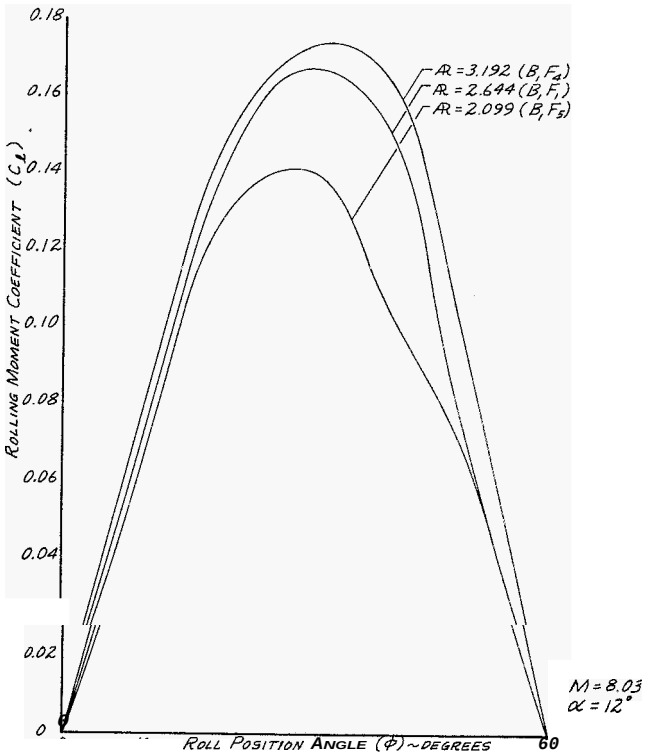

Figure 15. Effect of Aspect Ratio on Induced Rolling Moment
S_{REF} = Planform Area for One Fin
ℓ_{REF} = Body Radius

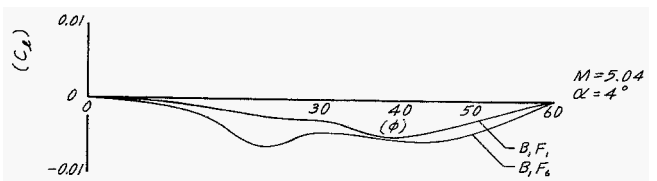

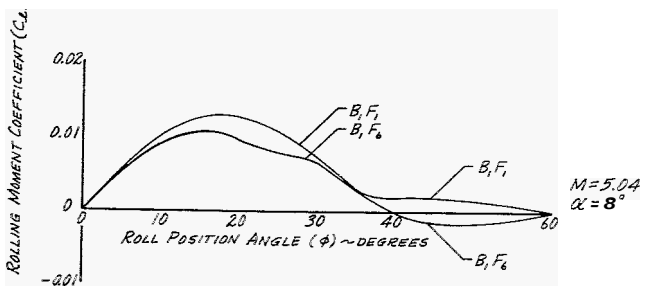

Figure 16. Effect of a Conical Flare on Induced Rolling Moment
S_{REF} = Planform Area of One Fin
ℓ_{REF} = Body Radius
$B_1 F_6$ has Conical Flair

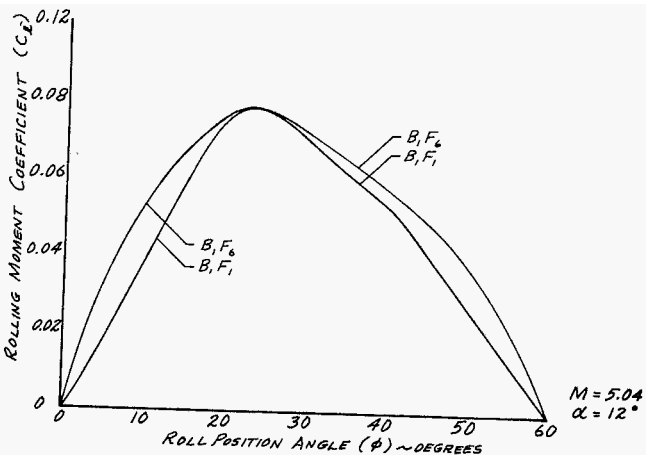

Figure 17. Effect of a Conical Flare on Induced Rolling Moment
S_{REF} = Planform Area of One Fin
ℓ_{REF} = Body Radius
$B_1 F_6$ has Conical Flair

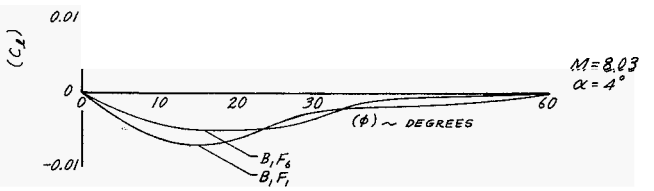

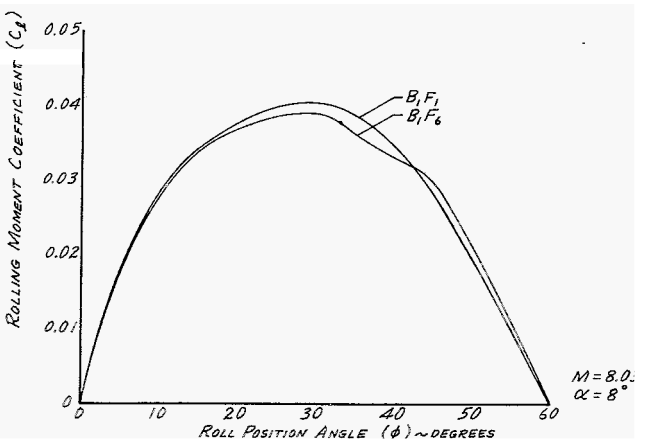

Figure 18. Effect of a Conical Flare on Induced Rolling Moment
S_{REF} = Planform Area of One Fin
ℓ_{REF} = Body Radius
$B_1 F_6$ has Conical Flair

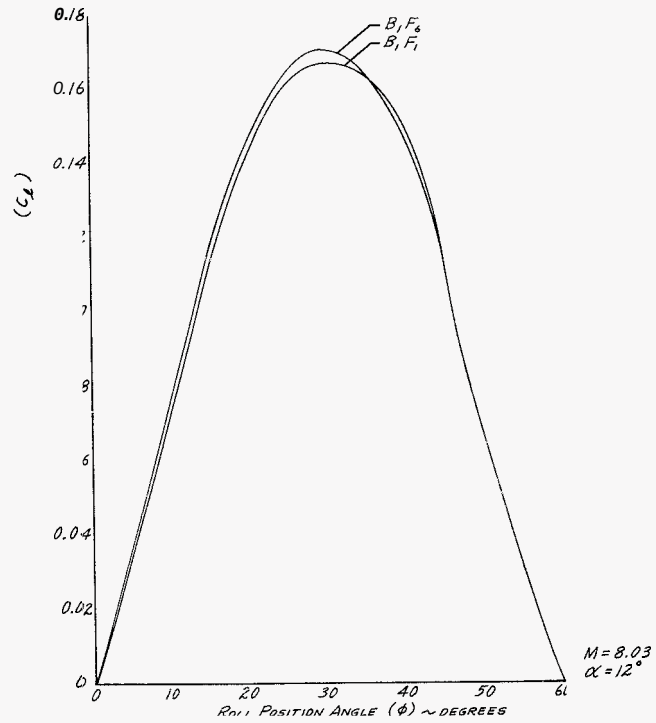

Figure 19. Effect of a Conical Flare on Induced Rolling Moment
S_{REF} = Planform Area of One Fin
ℓ_{REF} = Body Radius
B_1F_6 Has Conical Flair

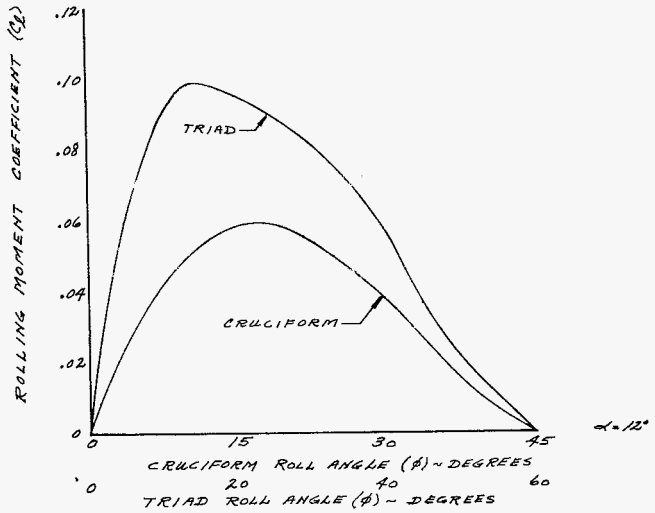

Figure 21. Comparison of Induced Rolling Moment for Triad Tail F_5 and Cruciform Tail A/B 350 at M=3.01

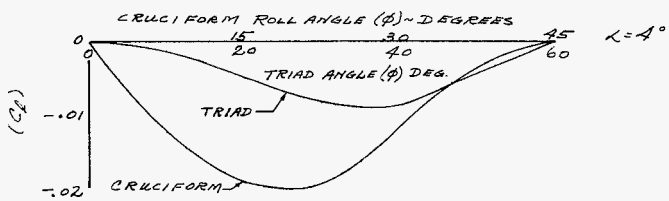

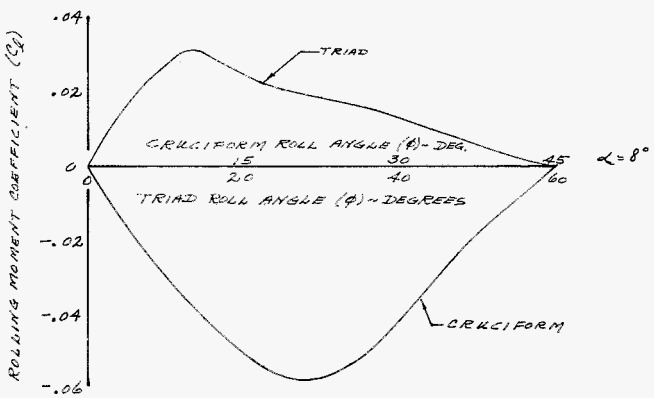

Figure 20. Comparison of Induced Rolling Moment for Triad Tail F_5 and Cruciform Tail A/B 350 at M=3.01

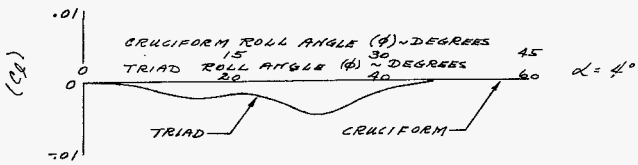

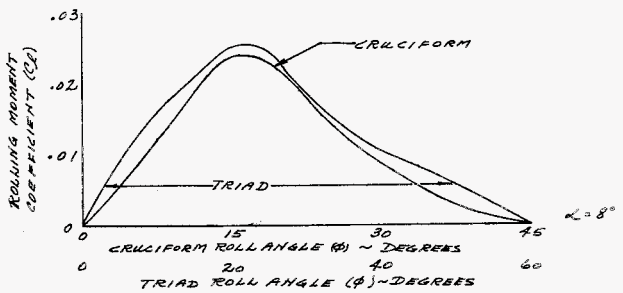

Figure 22. Comparison of Induced Rolling Moment for Triad Tail F_5 and Cruciform Tail A/B 350 at M=5.04

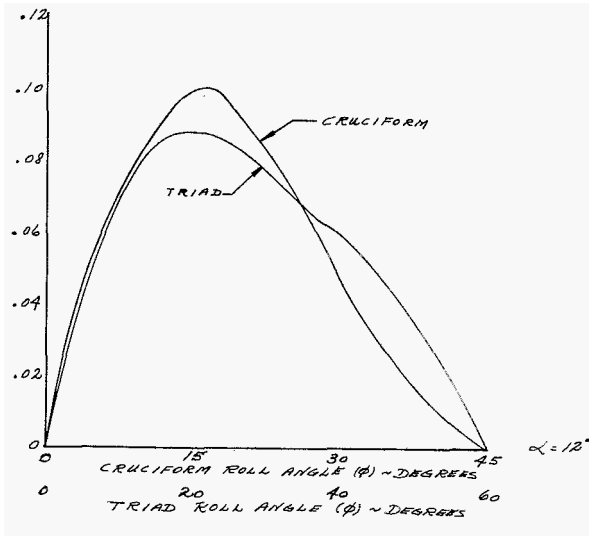

Figure 23. Comparison of Induced Rolling Moment for Triad Tail F_5 and Cruciform Tail A/B 350 at M=5.04

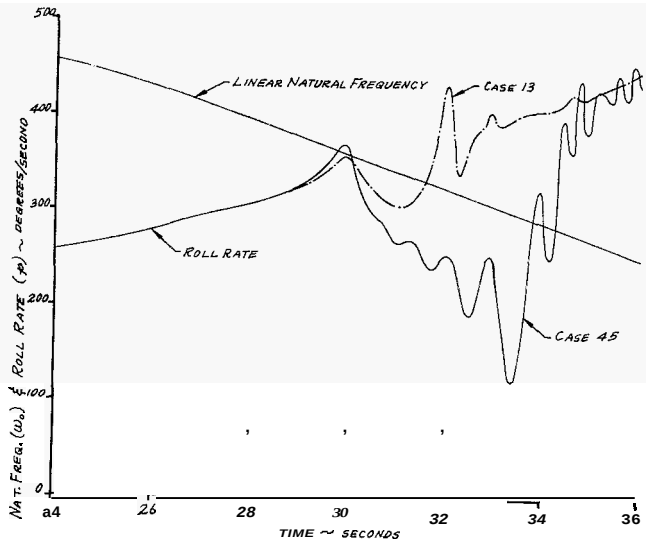

Figure 25. Aerobee 350 Roll Lock-in Study Roll Rate and Linear Natural Frequency vs. Time Cases 13 and 45

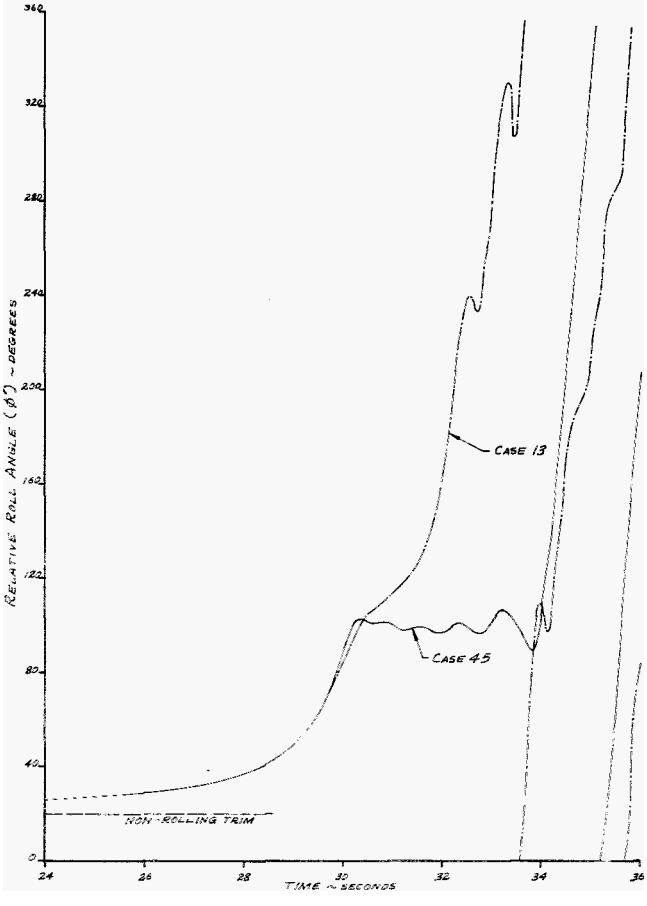

Figure 24. Aerobee 350 Roll Lock-in Study Relative Roll Angle vs. Time Cases 13 and 45

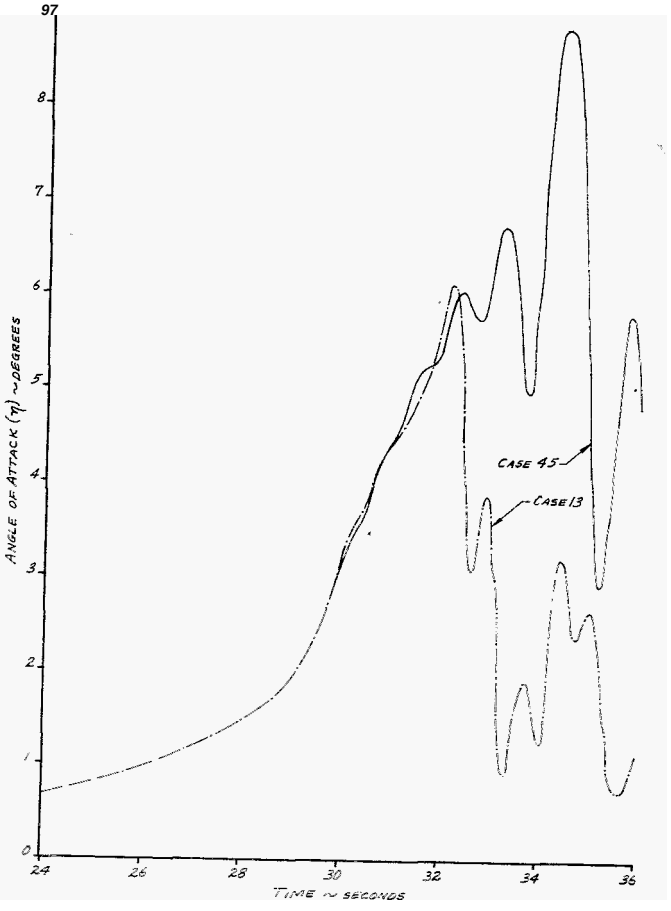

Figure 26. Aerobee 350 Roil Lock-in Study Angle of Attack vs. Time Cases 13 and 45